

MRI-Compatible, Transparent PEDOT:PSS Neural Implants for the Alleviation of Neuropathic Pain with Motor Cortex Stimulation

Young Uk Cho, Kyeongmin Kim, Ankan Dutta, Sang Hoon Park, Ju Young Lee, Hyun Woo Kim, Jieon Park, Jiwon Kim, Won Kyung Min, Chihyeong Won, Jaejin Park, Yujin Kim, Guanghai Nan, Jong Youl Kim, Taeyoon Lee, Hyun Jae Kim, Donghyun Kim, Jong Eun Lee, Byung-Wook Min, Il-Joo Cho, Bae Hwan Lee, HuanYu Cheng, Myeounghoon Cha,* and Ki Jun Yu*


Simultaneous monitoring of electrophysiology and magnetic resonance imaging (MRI) could guide the innovative diagnosis and treatment of various neurodegenerative diseases that are previously impossible. However, this technique is difficult because the existing metal-based implantable neural interface for electrophysiology is not free from signal distortions from its intrinsic magnetic susceptibility while performing an MRI of the implanted area of the neural interface. Moreover, brain tissue heating from neural implants generated by the radiofrequency field from MRI poses potential hazards for patients. Previous studies with soft polymer-based electrode arrays provide relatively suitable MRI compatibility but does not guarantee high-resolution electrophysiological signal acquisition and stimulation performance. Here, MRI compatible, optically transparent flexible implantable device capable of electrophysiological multichannel mapping and electrical stimulation is introduced. Using the device, neuropathic pain (NP) relief with a 30-channel electrophysiological mapping of the somatosensory area before and after motor cortex stimulation (MCS) in allodynia rats after noxious stimulation is confirmed. Additionally, artifact-free manganese-enhanced MRI of dramatic relief of pain-related region activity by MCS is demonstrated. Furthermore, artifact-free optogenetics with transgenic mice is also investigated by recording light-evoked potentials. These results suggest a promising neuro-prosthetic for analyzing and modulating spatiotemporal neurodynamic without MRI or optical modality resolution constraints.

1. Introduction

Electrophysiological diagnosis and treatment approaches using neural implantable devices have long been established as cornerstones for regulating brain functions.^[1–3] These tools have received great clinical attention in modulating neuronal propagation by applying a specific amount of current to a target brain region while recording biological signals from implanted sites.^[4–7] In particular, the high temporal resolution of the electrophysiological readout is specialized for analyzing pathological events of patients with rapidly changing neurodynamic. However, the local neural signal sensing method has a clear limitation in that it does not guarantee to observe the activity of the whole brain because it relies entirely on the recording area.^[8–10] Integrating electrophysiology with medical imaging, such as magnetic resonance imaging (MRI), for the simultaneous monitoring of neurophysiology and neuroimaging provides the ultimate solution to this issue.^[11–14] Furthermore, functional MRI and manganese-enhanced MRI (MEMRI), which serve as extensive

Y. U. Cho, S. H. Park, J. Y. Lee, H. W. Kim, J. Park, W. K. Min, C. Won, J. Park, T. Lee, H. J. Kim, D. Kim, B.-W. Min, K. J. Yu
Department of Electrical and Electronic Engineering
Yonsei University
Seoul 03722, Republic of Korea
E-mail: kijunyu@yonsei.ac.kr

K. Kim, G. Nan, B. H. Lee, M. Cha
Department of Physiology
Yonsei University College of Medicine
Seoul 03722, Republic of Korea
E-mail: mhcha@yuhs.ac
K. Kim, J. Kim, J. E. Lee, B. H. Lee
Department of Medical Science
Brain Korea 21 Project
Yonsei University College of Medicine
Seoul 03722, Republic of Korea

 The ORCID identification number(s) for the author(s) of this article can be found under <https://doi.org/10.1002/adfm.202310908>

DOI: 10.1002/adfm.202310908

functional investigations of the brain, are promising applications that generate great synergism with electrophysiological approaches.^[15–17] However, patients implanted with conventional bulk metal-based neural prostheses suffer from potential hazards due to the following three major issues: 1) medical image distortion from the inherent static magnetic field (B0) field for image acquisition, 2) brain damage from device heating by the radiofrequency (RF) field (B1) from MRI, and 3) potential risks of eddy current generated in conductive materials by gradient fields generated from equipped coils in MRI.^[18–22]

These problems arise because the clinical recording or stimulating electrodes are not free from intrinsic magnetic susceptibility and electrical conductivity with bulky size.^[23,24] For example, stainless steel electrodes exploited in conventional neural implants cause geometric signal distortion by magnetic fields from MRI due to their ferromagnetic properties. In addition, unwanted heating of the device by the induced RF field frustrate patients' safe lesion diagnosis.^[25] In summary, there is a pressing need for attractive neural interfaces capable of diagnosing and stimulating electrical neural activity with excellent spatiotempo-

ral resolution without electrode-induced imaging artifacts and tissue heating.

Conductive polymer (CP)-based soft implantable electrodes can easily mitigate the following clinical requirements with their diamagnetic properties with excellent mechanical characteristics.^[9,26–28] Unlike biocompatible metals such as gold (Au) and platinum (Pt) commonly used as recording electrodes,^[29] soft electronics based on CP have extremely low Young's modulus, minimizing the mechanical mismatch between brain tissue and the device.^[30] Among them, poly(3,4-ethylenedioxythiophene):poly(styrene sulfonate) (PEDOT:PSS) has received great interest in most neuroscience research due to its excellent electrical properties and biocompatibility.^[31–34] Typically, PEDOT:PSS is deposited on the surface of a stimulating electrode and has been extensively used for the measurement and modulation of neural signals.^[35–37] However, because a conventional electrode based on PEDOT:PSS has adopted a thin electroplating process on an additional metal layer, it is inevitable from the risk of potential MRI incompatibility of the pre-deposited metal. To solve this problem, several studies have been conducted to exploit micropatterning with a single layer of PEDOT:PSS through the solution process instead of the electroplating method.^[38,39] However, it is difficult to expect high-quality electrophysiological signals due to the low electrical conductivity of the single PEDOT:PSS layer. Some studies have attempted to enhance the electrical properties by modifying the molecular arrangement or structure of PEDOT:PSS but presented relatively poor performances compared to conventional implantable electrodes.^[40,41] Eventually, a neural interface by a special PEDOT:PSS treatment method without being affected by the magnetic field is needed.

Here, we present an MRI-compatible, optically transparent PEDOT:PSS-based electrocorticography (ECoG) grid (MRI-com PEDOT). The single-layer PEDOT:PSS microelectrode arrays (MEAs) demonstrated in the previous study^[38] is completely free of medical imaging artifacts by selecting a process that deviates from additional metal deposition. In this study, MRI-com PEDOT was immersed into heated ethylene glycol (EG) solution, significantly reducing electrochemical impedance and enhancing stimulation performance compared to those of electrodes subjected to EG treatment at room temperature.^[38] This study preliminarily investigated via waveguide simulation whether MRI-com PEDOT is less affected by the applied virtual magnetic field in each direction than the conventional Pt electrode. Imaging of the artifact property of MRI-com PEDOT and the Pt electrode is confirmed by 9.4T fast low-angle shot (FLASH) MRI of the primary somatosensory cortex (S1) of rats with device implantation. RF heating-induced temperature measurement and simulation tests are also conducted to certify the stability in the MRI of the device for future clinical applications. To confirm the multichannel electrophysiological mapping and electrical stimulation capabilities of the MEAs, decreased cortical activity of the neuropathic rat model was identified by mapping the signals from S1 after motor cortex stimulation (MCS). Distortion-free MEMRI results of neuropathic rats with MRI-com PEDOT provided results of pain relief in the somatosensory cortex and insular cortex (IC), with corresponding reduced neural activities on the surface area. Additionally, photoelectric artifact interrogation with channelrhodopsin-2 transgenic mice showed that the fully

A. Dutta, H. Cheng
Department of Engineering Science and Mechanics
The Pennsylvania State University
University Park, PA 16802, USA

A. Dutta
Center for Neural Engineering
The Pennsylvania State University
State College, University Park, PA 16802, USA

J. Kim, J. Y. Kim, J. E. Lee
Department of Anatomy
Yonsei University College of Medicine
Seoul 03722, Republic of Korea

W. K. Min, H. J. Kim
Electronic Device Laboratory
School of Electrical and Electronic Engineering
Yonsei University
Seoul 03722, Republic of Korea

Y. Kim, I.-J. Cho
Department of Biomedical Sciences
College of Medicine
Korea University
Seoul 02841, Republic of Korea

J. E. Lee
Brain Research Institute
Yonsei University College of Medicine
Seoul 03722, Republic of Korea

I.-J. Cho
Department of Anatomy
College of Medicine
Korea University
Seoul 02841, Republic of Korea

H. Cheng
Department of Materials Science and Engineering
The Pennsylvania State University
State College, University Park, PA 16802, USA

H. Cheng
Materials Research Institute
The Pennsylvania State University
State College, University Park, PA 16802, USA

K. J. Yu
Yonsei-KIST Convergence Research Institute
Yonsei University
Seoul 03722, Republic of Korea

transparent electrode array works favorably to integrate electrophysiology and optogenetics. This study provided a multimodal system that realizes clinically practical tools by minimizing potential hazards from patients with implants requiring medical images for translational lesion analysis.

2. Results and Discussion

2.1. Device Characteristics of MRI-Com PEDOT Electrode Array

MRI-com PEDOT is shown in a schematic illustration of its functionalities (Figure 1a). MRI-com PEDOT was designed to be applied primarily to two modalities: 1) robust electrophysiological signal mapping and modulation, 2) imaging distortion-free MEMRI acquisition. MRI-com PEDOT consisted of flexible and transparent 30 recording channels (electrode size: $50 \times 50 \mu\text{m}$; Figure S1, Supporting Information) and can measure evoked signals from the S1 of a rat. These recording channels were carefully designed, so the stimulating electrode (electrode size: $400 \times 400 \mu\text{m}$) was automatically positioned in the motor cortex according to the implanted site.

Although MRI-com PEDOT is implanted in the right cerebral cortex of a neuropathic rat model, it is invisible without image distortion on MRI when confirming the therapeutic effect of MCS. Moreover, the device is optically transparent; in medical imaging, it has favorable conditions for integrating electrophysiology and optical modality compared to the conventional Pt electrode array (Figure 1b; Figures S2 and S3, Supporting Information). For example, when controlling local neural activity using optogenetics, the decrease in light transmission efficiency due to opaque electrodes is significantly reduced. Also, it exhibits negligible photoelectric artifacts compared to conventional metal microelectrodes upon light stimulation. And the excellent electrical properties of the MRI-com PEDOT electrode were improved by post-treatment of the PEDOT:PSS layer on the heated EG (Figure 1c). EG treatment at room temperature guarantees the effect of enlarging the PEDOT:PSS grains and transforming the molecular linear arrangement.^[41,42] Additionally, electrodes heated at 100°C present enhanced electrical conductivity due to evaporation of water molecules present between the PEDOT:PSS dispersion.^[43] With this integrated device, we diagnosed and alleviated hind-paw pain in the allodynia rat model with different modalities. From the previous research that MCS is closely related to the relief of neuropathic pain,^[44–46] abnormal sensing of the neuropathic rat due to peripheral nerve damage was alleviated through MCS (Figure 1d).

To validate whether MRI-com PEDOT is sufficiently applied to multimodal applications, the electrical, optical, and mechanical properties of the electrodes were investigated. The electrode array was spin-coated with water-dispersed PEDOT:PSS solution (Clevios PH-1000) and micropatterned through ultrasonication lift-off followed by EG post-treatment (Figure S4, Supporting Information). In particular, the EG treatment introduced in the previous study was dipping the device at room temperature without heating EG.^[38] In this study, a dramatic enhancement of the electrical performance of the electrode array depending on the heating temperature of EG was observed (Figure S5, Supporting Information). EG treatment converts the coiled structure of pristine PEDOT:PSS into a linear arrangement, making the electron path-

ways to PEDOT:PSS grains flexible and improving conductivity. However, because water molecules in the dispersion continue to exist between polymer grains, it is difficult to expect significant electrical property improvement. When the film is immersed in EG and heated at 100°C for 30 min, the gap between polymer grains is reduced due to the evaporation of water molecules, and the charge hopping of electrons becomes smoother. This integrated processing results in interconnection with denser grains than simply dipping PEDOT:PSS in EG at room temperature, ensuring improved conductivity. To specify this result, the electrochemical impedance of 30 recording channels of MRI-com PEDOT (electrode size: $50 \times 50 \mu\text{m}$) was measured in phosphate-buffered saline (PBS; pH 7.4 at 37°C). Immersing the device into the heated-EG solution presented relatively consistent values, impedance values of $55 \pm 15 \text{ k}\Omega$ at 1 kHz among 30 channels, which were significantly lower than those ($95 \pm 15 \text{ k}\Omega$) of the electrodes that were treated with EG solution at room temperature (Figure 1e; Figures S5, S6, and S7, Supporting Information). The average difference between the two independent post treatment conditions was significant ($p < 0.05$), indicating the enhanced electrochemical properties from boiled ethylene glycol treatment has a 95% confidence level (Figure S8, Supporting Information). These results present an electrochemical impedance superior to carbon based electrodes such as carbon nanotube and graphene microelectrodes for brain recording.^[47–49] An electrochemical impedance spectra (EIS) of the stimulation electrode, an important factor for electrical stimulation, was also measured (Figure S9, Supporting Information). A larger surface area of the stimulating electrode showed a much lower impedance value ($25 \pm 5 \text{ k}\Omega$) even after EG treatment under the same conditions. Additionally, both the recording electrode and the stimulating electrode from MRI-com PEDOT showed stable electrochemical impedance maintenance for about 20 days (Figure S10, Supporting Information). The cyclic voltammetry (CV) of MRI-com PEDOT and Pt electrode array were also conducted, exclusively applied to the stimulating electrode (Figure 1f, Figure S11, Supporting Information). The alternating current from the stimulating electrode of MRI-com PEDOT exhibited an almost rectangular shape through induced various voltage sweep (Figure S12, Supporting Information). This indicated that EG treatment of PEDOT:PSS improved the electrochemical performance of the electrodes by further changing the surface roughness of the stimulating electrode and increasing the ion exchange area.^[38] For further stimulating performance comparison between the conventional Pt electrode array and the MRI-com PEDOT electrode array, the charge storage capacity (CSC) of each electrode was calculated using a CV curve. Among them, cathodic CSC is calculated as an area value when cathodic current is measured by a voltage sweep. As expected, it was confirmed that the MRI-com PEDOT electrode array had a better cathodic CSC value than the conventional Pt electrode array (Figure S13, Supporting Information). Charge injection capacity (CIC) value from MRI-com PEDOT was also acquired through voltage transient measurement (Figure S14, Supporting Information). CIC is a parameter that shows the limit on how much charge can be injected from the geometrical surface area of a given stimulating electrode. It is obtained by the current density (area of current pulse from time periods) until negative potential excursion (E_{mc}) and positive potential excursion (E_{ma}) reach the water window. As a result, when

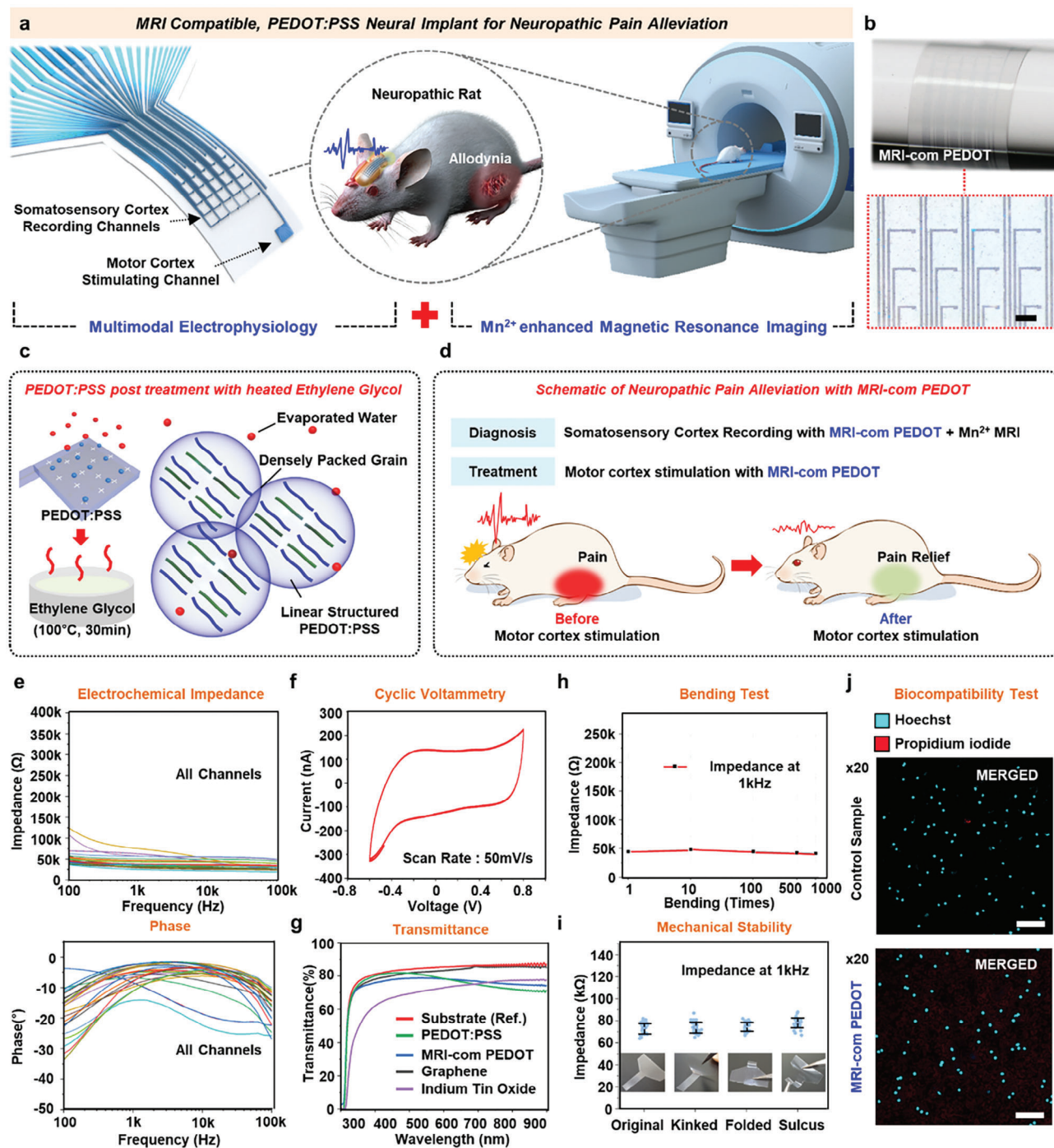


Figure 1. Device characteristics of MRI-com PEDOT. a) Schematic illustration of MRI-com PEDOT neural interface for integration of electrophysiology with magnetic resonance imaging (MRI). b) An image of MRI-com PEDOT wrapped around the cylindrical glassy rod (diameter, 5 mm). A red-dashed line presents the magnified image of an electrode array. Scale bar, 200 μm . c) Schematic illustration of PEDOT:PSS post treatment with heated ethylene glycol. d) Schematic illustration of neuropathic pain alleviation. Depending on the motor cortex stimulation, pain relief of the hind-paw was diagnosed with electrophysiological recording. e) 30-Channel electrochemical impedance spectra (EIS) and phase plot of MRI-com PEDOT. f) Cyclic voltammetry of MRI-com PEDOT (sweep range: -0.6 to 0.8 V, scan rate: 50 mV s^{-1} , sweep cycle: three times). g) Transmittance plots of candidates of transparent neural interfaces at a range of visible wavelengths (300–900 nm). PET (thickness: 25 μm) film on polydimethylsiloxane (PDMS)-coated glass substrate was used as a reference plot. h) EIS result of MRI-com PEDOT depending on the bending of the device onto the cylindrical rod (diameter: 5 mm). The average electrochemical impedance from each electrode channels at 1 kHz was measured. i) Mechanical stability test of MRI-com PEDOT. EIS values from 30 channels were measured from the four different structures (original, kinked, folded, and sulcus). j) Adult mouse cortical neuron cell viability analysis with device implantation. Bright sky blue-colored cells indicate cortical nuclei stained with Hoechst, and dark, red-colored cells indicate dead cells stained with propidium iodide. Scale bar, 50 μm .

a current pulse of 50 Hz and 2 mA intensity was applied, the CIC of the MRI-com PEDOT came out as 0.7 mC cm^{-2} . The reason why the ideal voltage drop did not occur is due to the delayed recovery period from capacitive characteristics of the PEDOT:PSS electrodes. To confirm whether the MRI-com PEDOT electrode array is damaged by continuous electrical stimulation, the electrochemical impedance change by repetitive current pulsing for 10 days was measured (Figure S15, Supporting Information). The parameters of the applied current (intensity: $50 \mu\text{A}$, frequency: 50 Hz, pulse width: $300 \mu\text{s}$) proceeded the same as the conditions for pain relief of the neuropathic model, and our electrode array showed negligible change of stimulating performance even for more than 10 days. On the other hand, in the case of the Pt electrode, a drastic increase in impedance was shown within about 30 to 40 min, which indicates damage to the electrode due to the dominant faradaic reaction from continuous pulsing. To compare MRI-com PEDOT to the materials used to fabricate transparent neural interfaces studied previously, the optical transparency of the device in the visible wavelength was analyzed (Figure 1g). Considering that the intrinsic transparency of the $25 \mu\text{m}$ polyethylene terephthalate (PET) film substrate was $\approx 85\%$, the films coated with pristine PEDOT:PSS and PEDOT:PSS-EG showed a high light transmittance of 71%. This transparency showed a constant light transmittance with almost no change even when measured over a long period of time (Figure S16, Supporting Information). In particular, the film deposited with indium tin oxide showed lower transparency than MRI-com PEDOT ($\approx 67\%$ in the visible wavelength).

The device bending test was also conducted to verify the mechanical stability of MRI-com PEDOT (Figure 1h). An electrochemical impedance change was observed when the device was repeatedly bent with a cylindrical rod of 5 mm diameter. Notably, no distinct variation in impedance was shown even at cyclic bending of electrodes over 1000 times. In addition, we checked whether there was an abrupt degradation in electrical characteristics while the electrode array applied various types of strain to the patterned substrate (Figure 1i). As expected, there was no significant change in the electrochemical impedance when the device was converted to kinked, folded, and sulcus structures. Finally, an in vitro cell viability test was performed to investigate whether MRI-com PEDOT could be applied in vivo without cytotoxicity (Figure 1j and Figure S17, Supporting Information). The degree of apoptosis of cortical neuron cells directly grown on the MRI-com PEDOT array was visualized by Hoechst and propidium iodide (PI) staining and observed by optical imaging. Conspicuously, dead cells were not observed in the control sample cultured without the device and in the sample cultured on the device (Figure S18, Supporting Information). To secure more reliable in vivo stability, our MRI-com PEDOT electrode array was implanted into somatosensory cortex of rats for an extended period and then the inflammatory reaction was evaluated (Figures S19 and S20, Supporting Information). Notably, lipid aggregation and granuloma formation are not seen, although a small amount of blood is observed that appears to be due to surgery. This result demonstrated that cell death at the site where the device is implanted is not related to MRI-com PEDOT, indicating a good agreement with the well-known biocompatibility of the soft PEDOT:PSS electrode.

2.2. In Vitro and In Vivo MRI Compatibility Test of MRI-Com PEDOT

The potential risks and key features of MRI-com PEDOT when neural implant patients undergo MRI are presented in Figure 2a. There are three main issues: 1) image distortion from magnetic susceptibility, 2) brain tissue damage from RF-induced heating, and 3) imaging artifact from eddy current. First, the magnetic susceptibility of the conventional neural interface is affected by the static magnetic field (B_0) applied by the MR scanner and causes imaging artifacts due to poor signal transmission to the receiver coil.^[23,50] The formula for how the magnetism of a material affects the surrounding magnetic field from MRI is as

$$\chi = J/B_0 \quad (1)$$

where χ is the magnetic susceptibility of materials, J is the internal polarization, and B_0 is the external field from the MRI. The diamagnetic MRI-com PEDOT has a negative susceptibility from the magnetic field (-0.0037), which indicates that PEDOT:PSS-EG acts slightly in the opposite direction to the applied field. In other words, the characteristics of MRI-com PEDOT, which hardly reacts to external magnetic fields, do not pose any problems obtaining medical images.

RF-induced heating from neural implants with MRI is directly affected by the specific absorption rate (SAR), which is expressed as

$$\int \frac{\sigma (|E_x|^2 + |E_y|^2 + |E_z|^2)}{2\rho} dV \quad (2)$$

where σ is the electrical conductivity of the tissue, ρ is the mass density of tissue, and E_{xyz} is the electrical field induced by the RF coil. SAR is the RF energy absorbed by the patient when the device is implanted, which is closely related to the heat applied to the brain.^[51,52] MRI-com PEDOT has relatively low electrical conductivity based on the same mass density compared to the conventional metal electrode; thus, the potential heating issue by RF can be minimized. Concerns about electrophysiological recording due to the relatively low conductivity of PEDOT:PSS-EG can be sufficiently overcome by the generation of double-layer capacitance between the electrode/electrolyte interface and the reduction in impedance due to the high surface area compared to metal. Last, the magnetic field by the gradient coil attached to the MR scanner generates an induced voltage around the inserted electrode. This induced voltage to the implanted electrode generates an eddy current, mainly caused by the closed-loop resistance of the electrode. The eddy current also indirectly causes imaging artifacts of MRI and tissue joule heating.^[20,53] To validate whether the device is suitable for integrating electrophysiology and MRI, simulation tests for potential hazard from brain tissue heating or imaging distortion from each electrode array (Pt and MRI-com PEDOT) were performed.^[54–56] The detailed set-up for bench test simulation is presented in Figure S21 (Supporting Information). First, SAR across the brain tissue from each electrode was shown in simulation test, which guarantees the safety of MRI-com PEDOT from the RF-induced heating (Figure S22, Supporting Information). To validate the temperature

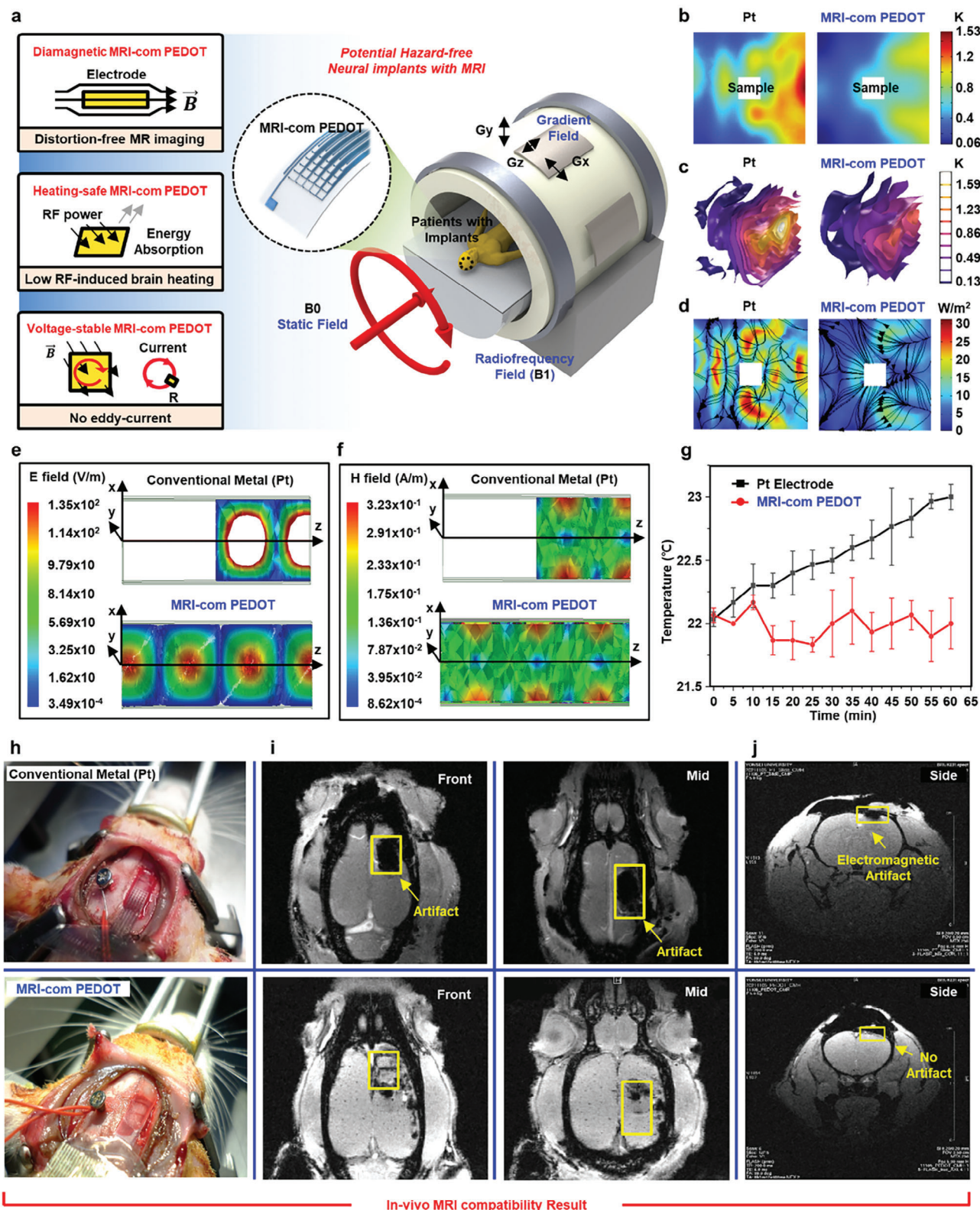


Figure 2. In vitro and in vivo MRI compatibility interrogation. a) Schematic illustration of potential hazards arising from patients with neural interface undergoing MRI. Parameters generated from the electrode array are displayed as red- and orange-colored bars, and parameters generated from the MRI unit are displayed as green-, blue-, and magenta-colored bars. b) Heatmap simulation of temperature incrementation of brain with each neural electrode. Cross-sectional view (taken midsection) of rise in temperature across brain tissue from Pt electrode (Left) and MRI-com PEDOT electrode

increase of the device within MRI, heatmap simulations were performed in both cross-sectional and contoured direction of the brain inducing the radiofrequency field (Figure 2b,c). Notably, the simulation result showed significant difference between Pt electrode and our MRI-com PEDOT, which indicates the much lower temperature increase of the electrodes from the magnetic field. And then, the total heat flux simulation within MRI was followed to specifically demonstrate the heat dissipation from each electrode (Figure 2d). The heat flow simulation was measured in watts per square meter (W m^{-2}), showing the transferred heat from each phantom electrode array in MRI. Our MRI-com PEDOT showed negligible heat dissipation even in the tissue closest to the electrode, while the conventional Pt electrode presented a high heat flux of 30 W m^{-2} around the phantom brain tissue. In addition, a simulation of electromagnetic performance using the Ansys HFSS tool was conducted to confirm which part of the electrode array-specific distortion is expected (Figure 2e,f). The simulation parameter was determined by magnetic susceptibility test of the MRI-com PEDOT electrode array (Figure S23, Supporting Information) and previous studies.^[57–59] We checked whether the field interfered with the electrode when the electric and magnetic fields were applied to a waveguide, placing the electrodes in the center of the waveguide. As a result, MRI-com PEDOT also did not interfere with the field applied to the waveguide, consistent with the simulation results where nothing was placed in the center of the waveguide (Figure S24, Supporting Information). However, the conventional Pt electrode did not pass through the induced electromagnetic field and resulted in blocking. This result showed that the applied magnetic field is attracted toward the material due to the perpendicularly placed paramagnetic Pt film and does not pass through the waveguide. This indicated that implanted Pt-based electrodes with paramagnetic properties could also cause image distortion by the static magnetic field during the MRI acquisition process is in agreement with the simulation result of electric field distribution and its permeability (Figures S25 and S26, Supporting Information). In vitro heating measurement with 0.9% agarose gel in MRI was followed to consider the risk of joule heating by the RF field. First, the device was slightly placed on the agarose phantom, and the temperature sensing probe was contacted on the device to observe the temperature change in real-time during the MRI operation (Figure S27, Supporting Information). As a result, the Pt electrode showed a temperature increase of $\approx 1 \text{ }^\circ\text{C}$ after 60 min from the MRI operation time, but the electrode array showed only a negligible change (Figure 2g). Before conducting animal experiments, to confirm that imaging distortion does not occur

when our MRI-com-PEDOT is applied to the MRI, the device was placed on the surface of 0.9% agarose gel and moved into a 9.4T MR scanner (Figure S28, Supporting Information). This study used FLASH MRI for the imaging distortion test, a way to clearly show the artifact of metal electrodes and fluid from the gradient echo. When scanning the identical agarose phantom model with the same number of frames, a dark blurred region was formed around the electrode in the conventional Pt electrode. In contrast, MRI-com PEDOT did not show any imaging artifacts, except around the edge of the device in the same frame. These data validated that MRI-com PEDOT is completely free from potential hazards caused by RF heat and image artifacts after device insertion. To demonstrate whether this result is equally applicable to the in vivo environment, both the conventional Pt electrode array and MRI-com PEDOT were implanted in the right cerebral cortex of rats, followed by MRI (Figure 2h). The reference wire and metal screw for electrophysiological signal readout were removed during the MRI distortion test. To minimize the imaging artifacts caused by the motion of the device, bone paste with dental cement was evenly applied to the skull. In the horizontal view images of the brain, the scanning angle of the MRI was slightly adjusted in consideration of object geometry-induced distortion (Figure 2i). When the scanning angle was tilted forward, a black patch from the signal void was observed around the motor cortex where the conventional Pt electrode was localized, whereas MRI-com PEDOT presented clear images. As expected, when the scanning angle returned to the normal direction perpendicular to the MRI field, image distortion was observed in the somatosensory cortex only when the Pt electrode was localized. The coronal view of the brain with the Pt electrode array also showed a blurred black area from electromagnetic image artifacts around the implanted site compared to that of MRI-com PEDOT (Figure 2j). The size of the distortion region obtained from the images with Pt and MRI-com PEDOT was scrutinized. As a result of three trials of MRI acquisitions, the image artifact size of the Pt electrode array was $\approx 0.6 \text{ cm}^2$, whereas the MRI-com PEDOT exhibited almost negligible artifacts (Figure S29, Supporting Information).

2.3. In Vivo Electrophysiology for Pain Alleviation of the Neuropathic Rat

In recent years, there have been studies on treating neuropathic pain caused by damage to the peripheral nerve. Several studies have reported that current stimulation with a certain

(Right). c) Simulation result of temperature increase of brain with each neural electrode. Rise in temperature as contours across the brain tissue with Pt electrode (Left) and MRI-com PEDOT electrode (Right). d) Simulation result of total heat flux within MRI from each neural implant. Result of heat flux magnitude and direction across the brain phantom from Pt electrode (Left) and MRI-com PEDOT (Right). e) Ansys HFSS simulation results of a waveguide inducing the electrical field. The conventional Pt electrode array and MRI-com PEDOT array were placed in the center of the waveguide. f) Ansys HFSS simulation results of a waveguide inducing the magnetic field. The conventional Pt electrode array and MRI-com PEDOT array were placed in the center of the waveguide. g) In vitro time-dependent temperature measurements of the device during MRI operation. The total measurement time was 65 min, and the temperature was checked every 5 min. Three individual samples were tested with both electrodes (Pt and MRI-com PEDOT). Error bars indicate standard deviation of the temperature increase of each 5 min interrogation of samples, and the lines indicate the average of temperature from three samples. h) Images of the implanted conventional metal (Pt; top) and MRI-com PEDOT (bottom) on the cerebral cortex of a rat model. i) In vivo MRI FLASH imaging results with implanted conventional metal (Pt; top) and MRI-com PEDOT (bottom). The MR scanning angle was changed from the "Front" (left) angle to the "Mid" (right) angle of horizontal views to distinguish whether the blurred areas were from artifacts or blood. Yellow-colored box indicates the device implantation site. j) Coronal slices of MRI acquisition with implanted conventional metal (Pt; top) and MRI-com PEDOT (bottom). Yellow-colored box indicates the device implantation site.

frequency and magnitude to the motor cortex suppresses neuropathic pain.^[60–62] However, diagnosing and treating neuropathic pain with multichannel electrophysiological signals has not been thoroughly studied. To confirm the effect of this electrical stimulation from MRI-com PEDOT, the electrode array was implanted onto the right cerebral cortex of neuropathic rats (Figure 3a). To ensure more accurate implantation coordinates, the electrode array was fixed with dental cement, and measurement was performed. A reference wire for neural recording was wound and connected to a metal screw on the left cerebral cortex (Figure 3b). First, a 30-channel electrode array was placed in the somatosensory cortex of the tibial-sural nerve transection model to record the evoked response seen when allodynia is accompanied by hind-paw stimulation (HPS) (Figure S30, Supporting Information). One stimulating electrode in MRI-com PEDOT was directly placed over the motor cortex, inducing a series of currents (biphasic symmetric, 50 Hz, 50 μ A, pulse width: 300 μ s) on the brain surface. To investigate whether the activity of the somatosensory cortex by the neuropathic pain model after MCS is reduced, 30 recording channels again measured the electrophysiological signal changes from the somatosensory cortex (Figure S31, Supporting Information). HPS and neural recording were performed simultaneously for 15 min, and the evoked potential that appeared after the stimulation onset was recorded from a 30-channel electrode array. MCS was followed for 30 min. As in the previous process, the pain relief effect from HPS in the somatosensory cortex was validated by real-time ECoG. The detailed experimental protocol is shown in Figure 3c. Specifically, among all channels, 18 on the right side of the electrode arrays were placed in the hindlimb region of the somatosensory cortex, so the evoked response ($n = 4$) by noxious stimulation was more prominent (Figure 3d and Figure S32, Supporting Information). The mean local field potentials (LFPs) in the somatosensory cortex hindlimb after HPS (intensity: 3 mA, frequency: 0.2 Hz, biphasic symmetric) is shown in Figure 3e. Notably, sham models showed an evoked potential of ≈ 200 μ V after HPS with and without MCS. In contrast, the neuropathic pain model before MCS showed a remarkably high evoked response (≈ 450 μ V) after stimulus delivery despite the same current level applied to the hind-paw for four additional models (Figure S33, Supporting Information). This indicated that the model with neuropathic pain has a greater pain activity in the central nervous system even after the same intensity of noxious stimulation. Surprisingly, the somatosensory response to HPS shown in the neuropathic pain model after MCS was significantly reduced. The frequency spectra of HPS evoked potentials before and after MCS also showed a clear intensity difference (Figure S34, Supporting Information). The average LFPs at this time were almost not significantly different from the baseline response, suggesting that the brain activity related to nociception in the hindlimb returns to a normal level. Additionally, the evoked activity of the somatosensory cortex was measured depending on the current intensity of HPS (1, 3, and 5 mA; Figure 3f and Figure S35, Supporting Information). All evoked potentials were detected ≈ 40 ms after HPS onset, exceptionally showing the negligible response from the stimulation of 1 mA. The evoked potentials for HPS exhibited before MCS increased slightly as the intensity of noxious stimulation increased. In contrast, the somatosensory response from the brain after MCS showed dramatically lowered LFPs around 50 μ V by the

current stimulation compared to the reference response. These results demonstrated that neuropathic pain could be alleviated by MCS, and its therapeutic effect can be confirmed by the electrophysiological recording of the brain. Figure 3g presents the 30-channel electrophysiological mapping of evoked LFPs by HPS before and after MCS in a neuropathic pain model obtained from MRI-com PEDOT. The 30-channel color map based on changes in brain waveforms after 100 ms from HPS onset shows pain alleviation by MCS more visibly. High LFPs (>500 μ V) that appeared before MCS significantly decreased in amplitude after MCS. In particular, the electrode array showed more prominent neurodynamic activity in the brain region accompanying hindlimb sensation among the somatosensory cortex, which agrees with the existing anatomical interpretation.

2.4. MEMRI for Examining Neuropathic Pain Alleviation

MRI-com PEDOT has imaging invisibility optimized to show that allodynia caused by HPS in the deep brain can be suppressed by MCS with MEMRI. To authenticate this characteristic, the device was implanted into the right cerebral motor cortex of a neuropathic rat (Figure 4a). When HPS is conducted first, neural activity is markedly expressed in hindlimb region of the somatosensory cortex (S1HL) and IC. Because the manganese solution is injected from the external carotid artery (ECA) of the right ventral aspect of the neck, neural activity in the right hemisphere of the brain is observed (Figure S36, Supporting Information). Figure 4b shows an image of the experimental setting for MCS during the MEMRI process. The stimulating electrode was placed on the motor cortex, and a ground wire was implanted in the neighboring area to bypass the induced current. Dental cement is applied to the entire skull, including electrodes and ground wire, to firmly position the electrode array. In the neuropathic pain model and the MCS model, MRI-com PEDOT is implanted, but only the process of whether it undergoes the MCS process is different (Figure 4c). The MCS protocol was conducted in the same way as the parameters (biphasic symmetric, 50 Hz, 50 μ A for 30 min) used for pain alleviation through the previous electrophysiological approach. The detailed experimental process for MEMRI with MCS of neuropathic pain is illustrated in Figure 4d. After implantation of the stimulating device and tube insertion for manganese injection, neuropathic rats underwent MCS immediately. Afterward, the process of entering the scanner for MRI acquisition is followed. Mannitol injection is performed before manganese injection for blood-brain barrier (BBB) opening during HPS. Due to the rapid diffusion of manganese ions, MEMRI proceeded simultaneously with mannitol injection. Evoked neural activity by external stimuli appears as a bright white color by manganese ions, which show a strong contrast effect by shortening the T1 time of water protons in MRI. As expected, MRI-com PEDOT did not produce any image distortion at the implanted site and its immediate vicinity (Figure S37, Supporting Information). Brain regions activated by HPS in neuropathic rats are shown in sequential frames from 1 to 4 (Figure 4e). For Frame 1, S1HL activation was the most conspicuous image slice, and high manganese diffusion in the IC region was shown in Frame 2. Surprisingly, regions showing high activity for each frame presented a dramatic reduction after MCS from each repetitive

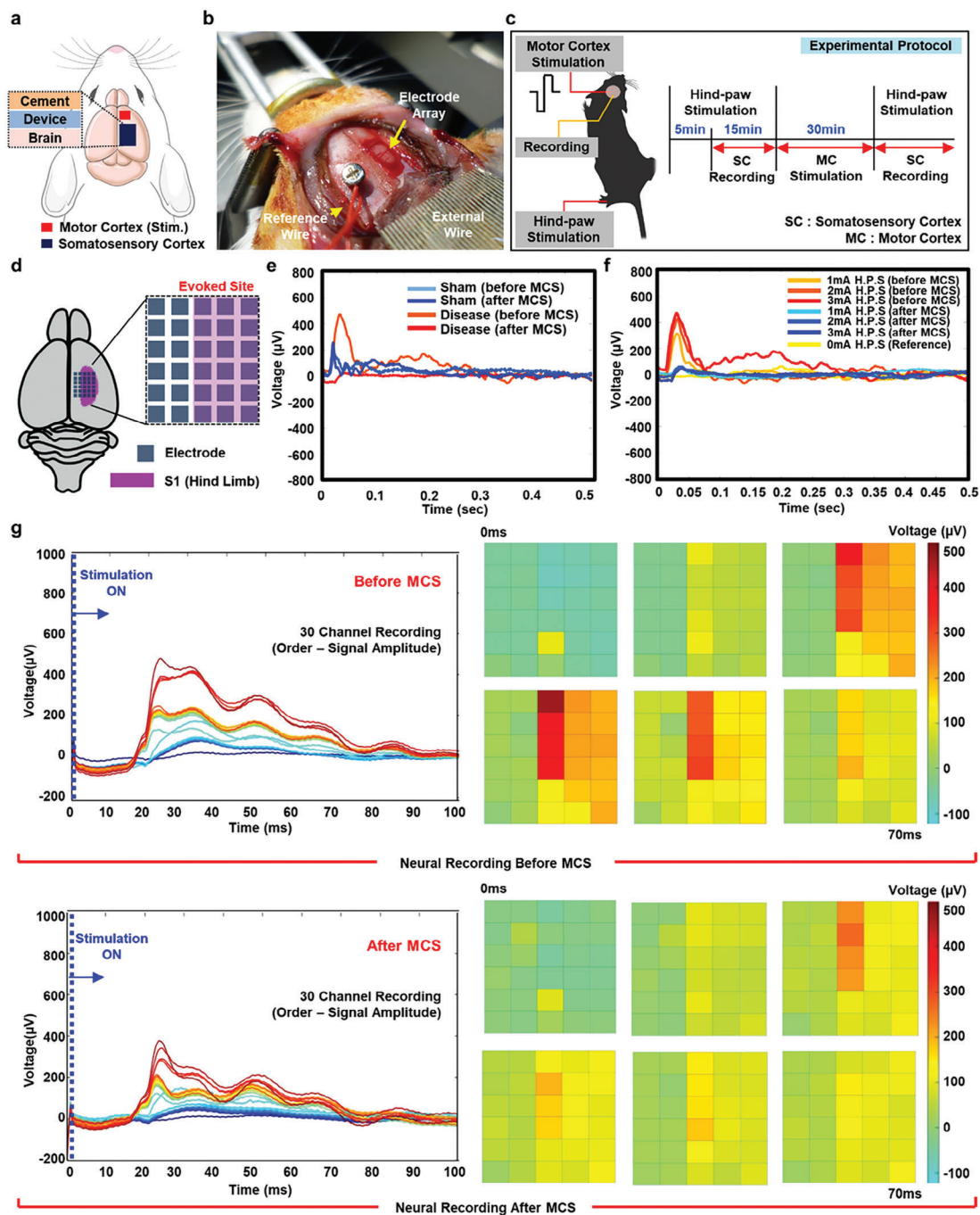


Figure 3. In vivo electrophysiological recording/stimulation for alleviating neuropathic pain. a) Schematic illustration of the implantation site of an experimental rat model. A stimulating electrode and recording channels were placed on a motor cortex and somatosensory cortex of a rat, respectively. b) Experimental set-up for electrophysiological recording/stimulation of the rat brain. The anisotropic conductive film was connected to the device to receive a neural signal from the sensing site. A reference wire was bent around the embedded metal screw. c) Experimental protocol for in vivo recording/stimulation. HPS was conducted in accordance with somatosensory cortex neural recording. MCS was followed for 30 min, and neural activity was remeasured to compare the therapeutic effect of MCS. d) Illustration of the implanted site of MRI-com PEDOT. A 30-channel electrode array was implanted onto the right cerebral cortex of a rat brain. The purple-colored box indicates the area of electrodes distributed in the hindlimb region of the somatosensory cortex (S1HL). e) Graphs of changes in evoked potentials before and after MCS in the sham rat and the tibial-surral nerve transection rat (neuropathic pain) model. All four plots were calculated as the average of 30-channel recording electrodes of MRI-com PEDOT voltage values, and the onset time of HPS for evoked potentials was measured based on 0 s. f) Graph of the somatosensory evoked potential of the neuropathic rat model according to current stimulation intensity of HPS and presence or absence of MCS. The bright yellow plot is the neural signal value when HPS was applied at 0 mA (sham/reference). g) (Left) Representative 18-channel electrophysiological signals from the hindlimb region before/after MCS with HPS. (Right) 30-Channel color mapping result of electrophysiological signals from the somatosensory cortex before/after MCS with HPS.

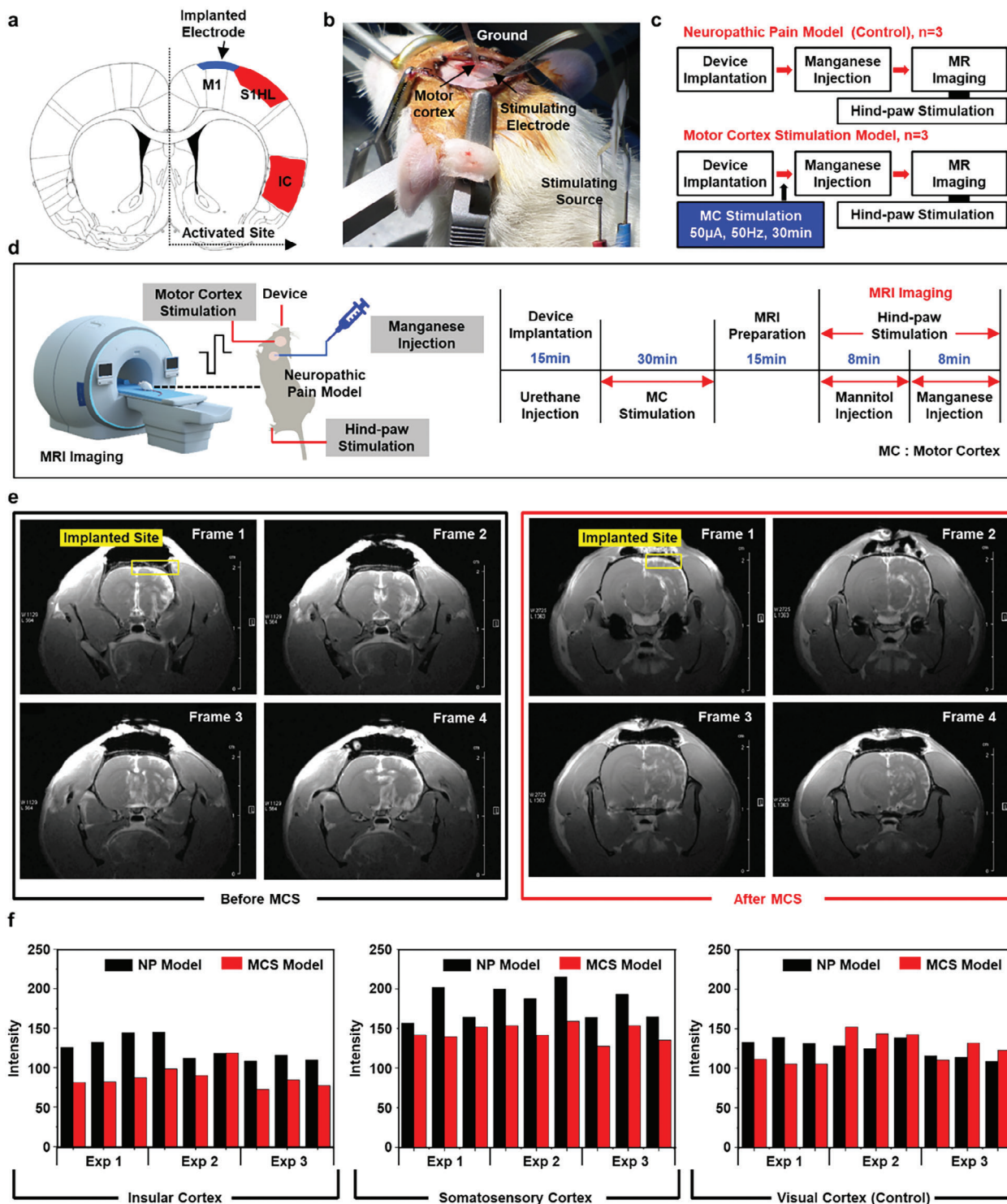


Figure 4. MEMRI for investigating the therapeutic effect of MCS on neuropathic pain. a) Illustration of regions of interest (S1HL and IC) of the brain with neuropathic pain. The blue-colored area depicts the implantation site of MRI-com PEDOT. The stimulating electrode was directly contacted on the right side of the motor cortex (M1) of the brain. b) Experimental settings of in vivo MCS of a neuropathic pain rat. The ground electrode was implanted in the vicinity of the M1 to bypass the induced current. c) Detailed procedure of in vivo experiments with the neuropathic pain model (control) and the MCS model. d) Experimental protocols for MEMRI with HPS. To pass the manganese ion through the BBB, mannitol administration was first conducted. e) Coronal images of MEMRI of the neuropathic pain model without (left) and with (right) MCS. To distinguish the activated regions, the expected activation regions were presented in four frames. The yellow-colored box indicates the MRI-com PEDOT implantation site. f) Neuronal activation intensity of the somatosensory cortex (left), IC (middle), and visual cortex (right) plot before/after MCS. The activation intensity from the visual cortex of rats was used as a reference region, independent of MCS. All intensity from the brain was tested with three neuropathic models ($n = 3$).

experiment with other neuropathic pain models (Figures S38 and S39, Supporting Information). The decreased diffusion of manganese ions into all regions involved in pain, except for the uppermost layer of the S1HL region, indicates that electrical stimulation of the motor cortex in MRI-com PEDOT is substantially correlated with pain relief. The manganese ion-enhanced region (a bright white region in MRI) was compared to the neuropathic pain model (control) and the MCS model (Figure S40, Supporting Information). Two brain regions (somatosensory cortex and IC) were chosen to confirm the effectiveness of the device for neuropathic pain alleviation. The visual cortex, an independent region from this experiment, was exploited as a reference region for manganese ion activation. As a result of confirming the pain-relieving effect of MCS in three rats for each brain region, decreased neural activity in prominent regions of interest was observed in all models (Figure 4f). In contrast, as expected, no significant difference was observed between the neuropathic pain model and the MCS model in intensity in the visual cortex, which requires independent neural activity regardless of the presence or absence of MCS. To visualize an analgesic effect more clearly, the statistical significance of the data between the two groups was verified using an unpaired *t*-test (Figure S41, Supporting Information). As a result, the average difference between the two independent groups was significant ($p < 0.05$), indicating that the neuropathic pain treatment effect by stimulation of the MCS models has a 95% confidence level.

2.5. In Vivo Simultaneous Electrophysiology with Optogenetics

Besides brain electrical stimulation, optogenetics-based neuron-specific modulation for further neuroscience research has greater synergy when accompanied by electrophysiological approaches.^[63–65] However, when light energy of a certain frequency is applied to the surface of the electrode, a photoelectric potential is generated by the exerted charge.^[65,66] This voltage is recorded together when measuring electrophysiology through electrodes and is combined with actual neural activity signals to cause signal contamination. For transparent electrodes, the total amount absorbed photon energy is small, resulting remarkably reduced photoelectric artifact. The optical transparency of MRI-com PEDOT is compatible with medical images and integration with optogenetic stimulation. Before in vivo experiment for simultaneous electrophysiology with optogenetics, we conducted artifact interrogation in vitro (Figure S42, Supporting Information). Notably, it was confirmed that our MRI-com PEDOT did not significantly cause signal contamination by light even with 1 and 5 Hz laser stimulation compared to Pt electrode (Figure S43 Supporting Information). To confirm the simultaneous neural recording with optogenetics feasibility of MRI-com PEDOT, the device was implanted over the somatosensory cortex of Thy1-ChR2-YFP mice (Figure 5a and Figure S44, Supporting Information). LFPs evoked by the blue laser of 473 nm were compared to the conventional Pt electrode and MRI-com PEDOT. A picture of 30 recording channels implanted in the somatosensory cortex of a transgenic mouse is shown in Figure 5b. The conventional Pt electrode array visually blocked the entire vicinity of the electrode placement due to its opaque nature, whereas the electrode array exhibited a see-through image. This result was closely related to

the amount of light transmission directly through the electrode during optogenetic stimulation, indicating that neurons in the target region can be modulated more efficiently even with the same light intensity. An optical fiber (diameter: 105 μm , duration: 50 ms, 2.5 Hz) was placed directly above the recording site of each electrode to figure out whether the blue laser could efficiently stimulate the neurons underneath the device (Figure 5c). As expected, the conventional Pt electrode array showed negligible evoked LFPs in all areas of 30 channels regardless of the vicinity of the electrode where stimulation was performed (Figure 5d; Figures S45 and S46, Supporting Information). In contrast, MRI-com PEDOT exhibited the most prominent light-evoked LFPs in the stimulated region. At the same time, MRI-com PEDOT showed high light transmission efficiency compared to the Pt electrode. In electrophysiological signals recorded by the Pt electrode array, especially, an additional peak was observed at the laser stimulation onset, which are contaminated signals caused by photoelectric artifacts. Photoelectric artifact refers to the voltage by electron emission when the light above the energy level where electrons remaining on the metal surface can be excited is applied. To investigate the electrophysiological signal contamination caused by this artifact, LFPs were measured while applying a blue laser to the electrode surface in wild-type (WT) mice whose neural activity was not affected by light (Figure 5e). In the conventional Pt electrode and MRI-com PEDOT, a distinct evoked response was not observed in the unilluminated electrode of the blue laser, whereas striking photoelectric artifacts were observed in each laser onset in the Pt recording electrode where the laser was illuminated. This result suggested that LFPs from WT mice by electron energy from the surface of the Pt electrode act as a noise in the biological signal. In contrast, MRI-com PEDOT did not cause any significant signal contamination regardless of whether light was stimulated, verifying the performance as a multimodal device.

3. Conclusion

This study dealt with the introduction of a transparent, implantable electrode array that can diagnose and treat the neuropathic pain model without any obstacles in the integration of three modalities (electrophysiology, MRI, and optogenetics). MRI-com PEDOT, which had better electrical properties through the post-treatment of the heated-EG, showed remarkably smaller artifact size and negligible RF-induced heat in MRI acquisition compared to conventional Pt electrodes. Pain alleviation through MCS in the neuropathic pain model with HPS was confirmed by 30-channel electrophysiological recording and stimulation of MRI-com PEDOT. Furthermore, through MEMRI after device implantation, the treatment effect by confirming the decrease in the activation of the pain-related region in the deep brain after MCS was verified. Finally, the optically transparent MRI-com PEDOT was free from photoelectric artifacts and demonstrated the feasibility of fusion of neuromodulation and electrophysiology using optogenetics. To be applied as a future work for chronic clinical application, further studies on encapsulation layer for the electrode array must be preceded, resulting in the device malfunction within 20 days. In addition, to apply this device to other disease models that require high frequency electrical stimulation, enhanced properties of stimulation performances are potentially

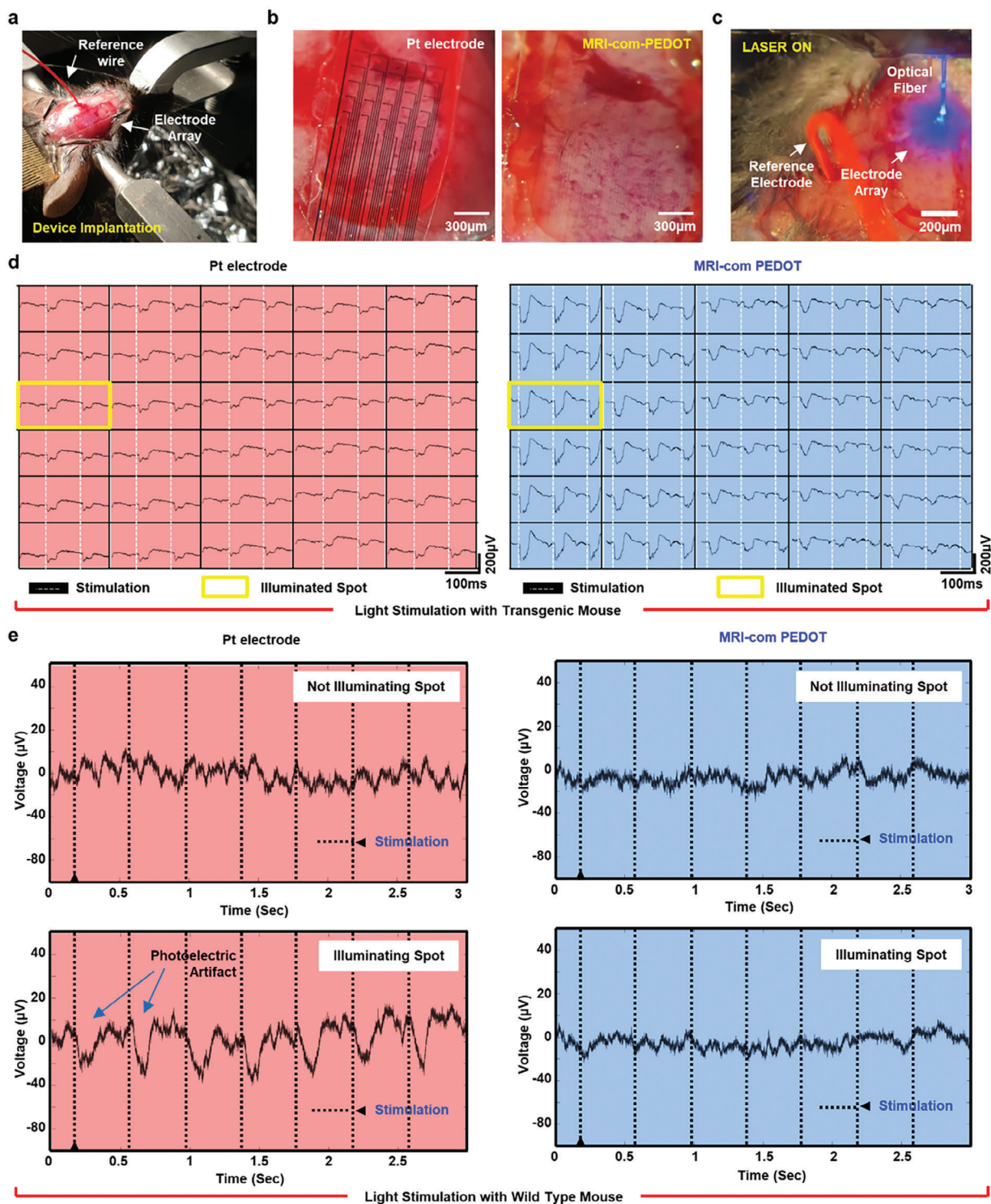


Figure 5. In vivo electrophysiological recordings for photoelectric artifact interrogation of MRI-com PEDOT. a) Image of device implantation. MRI-com PEDOT was implanted into the right cerebral cortex of a transgenic mouse. b) Optical images of implanted conventional Pt electrodes (left) and transparent MRI-com PEDOT (right). Scale bar, 300 μm . c) Image of a magnified image of optogenetic stimulation. Blue laser (470 nm, fiber diameter: 105 μm) was induced directly on the surface of a recording site of an electrode. Scale bar, 200 μm . d) 30-Channel electrophysiological recordings with optogenetic stimulation of a transgenic mouse with the conventional Pt electrode array (left) and MRI-com PEDOT (right). The white dashed line indicates the laser stimulation onset. The yellow-colored box presents the blue laser-illuminated spot. e) Electrophysiological signals from wild type mouse with blue laser stimulation. To authenticate that the fluctuating signals are from photoelectric artifacts, the results were presented in non-illuminating and illuminating spots. The black dashed line indicates the laser stimulation onset in the conventional Pt electrode array (left) and MRI-com PEDOT (right).

more required. However, MRI-com PEDOT presents a basic platform that can serve as a complementary multimodal system for unprecedented diagnosis and therapy in neuroscience research and other clinical applications between electrophysiology complementary multimodal systems.

4. Experimental Section

Material Preparation: PET substrate film (25 μm ; ES301230) was purchased from GFM Korea, PDMS was purchased from Dow Corning (USA), 1.3 wt% PEDOT:PSS aqueous dispersion in H_2O (Clevios PH-1000) was purchased from Heraeus, EG (99.5%; 107-21-1) was purchased from Duxsan Integrated Science, SU8-0.5 photoresist and photoresist developer was purchased from K1 Solution (South Korea), and AZ5214 photoresist and photoresist developer was purchased from AZ Electronic Materials (USA).

Fabrication of MRI-Com PEDOT Electrode Array: A 23 μm PET film was first slightly laminated onto the glass coated with PDMS. The positive photoresist AZ5214 was spin-coated on the PET substrate (rotation speed: 2000 rpm, soft curing time: 2 min at 110 $^\circ\text{C}$), and ultraviolet (UV) exposure (power: 14 mW, exposure time: 8 s) through the photomask was followed. An additional 3 min of curing the substrate at 120 $^\circ\text{C}$ was proceeded to establish the reverse pattern. After 14 s of full exposure to UV, the substrate was immersed in a developer solution. The patterned device was subjected to oxygen (O_2) plasma treatment through reactive ion etching. PEDOT:PSS (Clevios PH-1000) solution was spin-coated on the treated substrate, and the solution curing process (110 $^\circ\text{C}$, 10 min) came before the liftoff. The device underwent ultrasonication liftoff, remaining the electrode interconnect lines and recording sites with PEDOT:PSS. After the electrode patterning, the device was immersed in the 90 $^\circ\text{C}$ EG solution for 30 min. The remnant EG was washed with isopropyl alcohol for 2 min. For encapsulation, the SU8-0.5 photoresist was spin-coated on the patterned device (rotation speed: 3000 rpm, soft curing time: 2 min at 100 $^\circ\text{C}$), and UV exposure (power: 14 mW, exposure time: 6 s) was followed. By immersing the resist developer (1 min 30 s), the recording site of the electrode array was exposed. After the hard curing process (120 $^\circ\text{C}$, 2 h), MRI-com PEDOT fabrication was achieved.

Fabrication of the Conventional Pt Electrode Array: The Pt electrode array was fabricated on a PET film substrate. The positive photoresist AZ5214 was spin-coated on the PET substrate (rotation speed: 2000 rpm, soft curing time: 2 min at 110 $^\circ\text{C}$), and UV exposure (power: 14 mW, exposure time: 8 s) through the photomask was followed. An additional 3 min of curing the substrate at 120 $^\circ\text{C}$ was proceeded to establish the reverse pattern. A 30 nm Pt layer was deposited by the ion-beam sputter (ISB-1000, Infovion). Ultrasonication liftoff of the device for the remaining recording electrodes was followed. The encapsulation layer was formed by spin-coating SU8-0.5 (rotation speed: 3000 rpm, soft curing time: 2 min at 100 $^\circ\text{C}$). Finally, the device was fully cured at 120 $^\circ\text{C}$ for 2 h.

EIS Measurement of MRI-Com PEDOT: EIS measurement was conducted with Gamry Reference 600+ potentiostat (Gamry Instruments). For more accurate measurements, a three-electrode method consisting of Ag/AgCl reference electrode, Pt wire counter electrode, and MRI-com PEDOT working electrode was adopted. First, after all, three electrodes were immersed in PBS (pH 7.4, 36 $^\circ\text{C}$), the charge change between the electrolyte and the electrode interface according to the frequency sweep was confirmed.

CV Characterization of MRI-Com PEDOT: The CV test was performed with Gamry Reference 600+ potentiostat and proceeded in the same way as the electrochemical impedance interrogation in three-electrode configurations (Ag/AgCl reference electrode, Pt wire counter electrode, and MRI-com PEDOT working electrode). The voltage sweep of the working electrode was performed in the range of -0.6 to 0.8 V, and the electrode scan rate was 50 mV s^{-1} . The current direction and magnitude from the electrode, which varies according to the potential sweep, were conducted for three sweep cycles. The results stabilized during the potential sweep among these data were graphed. In the case of charge storage capacity,

it was obtained through cyclic voltammetry of MRI-com PEDOT. To characterize the performance of the stimulating electrode, current density was calculated through voltage sweeping (-0.6 – 0.8 V) within the water window. Among them, cathodal charge storage capacity (CSCc) can be obtained as the time integral value of cyclic voltammetry according to the time of cathodic current. The corresponding calculation is as follows.

$$\text{CSC} = \frac{1}{S} \int_{t_1}^{t_2} I(t) dt \quad (3)$$

S = geometrical surface area of the electrode

t_1 = Beginning of the voltage sweep

t_2 = End of the voltage sweep

I = current (A)

$$\text{CSC} = \frac{1}{S\nu} \int_{E_1}^{E_2} I(E) dE \quad (4)$$

ν = scan rate (V s^{-1})

E_1/E_2 = cut-off potentials

Here, S indicates the current-delivered area of the electrode used as the cortex stimulation in the neural implant, and T_1 and T_2 indicate the start and end values of the voltage sweep, respectively. Here, since the volume that can store charge is a measure of the amount of charge per unit area, it varies according to the sweep scan rate at which cyclic voltammetry is formed. The CSCc was calculated with obtained absolute integral of the CV plot through a graph analysis tool (Origin pro.2022b).

Voltage Transient Measurements: For voltage transient measurement, cathodic leading, bi-phasic, symmetric current pulse (intensity: 2 mA, frequency: 50 Hz, pulse width: 300 μs) was applied in the PBS (pH: 7.4), across the working electrode (MRI-com PEDOT). The current pulse was provided through the Intan recording system (Intan RHS M4200; Intan Technologies, Los Angeles, CA, USA). The Ag/AgCl electrode was used for the reference electrode, and both working and reference electrode were connected to the data acquisition system (NI PXIe, NATIONAL INSTRUMENTS CORP) to record the applied signals. From the voltage transient plot, E_{ipp} indicates the initial bias level from the induced current, ΔV indicates the total voltage drop of the electrode. V_a presents the access voltage for the ohmic drop and ΔE_p indicates the polarization of the electrode. E_{mc} and E_{ma} presents the maximum negative potential excursion and positive potential excursion, respectively. For cathodic leading current induced result, the maximum negative potential excursion (E_{mc}) should be within the water window range (-1.6 – 0.7 V) of MRI-com PEDOT. To obtain CIC of MRI-com PEDOT, E_{mc} of MRI-com PEDOT was calculated by the following formula.

$$E_{\text{mc}} = E_{\text{ipp}} + \Delta E_p = E_{\text{ipp}} + (\Delta V - V_a) \quad (5)$$

From the plot, E_{mc} value was -1 V, and this value was in the range of water reduction limit potential (-1.6 V). The charge injection capacity was calculated from acquiring the area of the current pulse (current density), dividing the value with the geometric surface area of the stimulating electrode ($400 \mu\text{m} \times 400 \mu\text{m}$).

Transmittance Measurements: The light transmittance of all electrode arrays was measured with a UV-visible spectrophotometer (V650-JASCO). The slow speed of the samples was 2000 nm min^{-1} , and the scanning range of the wavelength was from 300 to 900 nm. The reference mode was conducted by the slide glass sample.

Device Bending Test: For the bending test, the device was repeatedly wound on a cylindrical rod with a diameter of 5 mm and released. Electrochemical impedance was remeasured as often as the number of windings on the rod, and the observed data at 1 kHz among the scanning frequencies (1–100 kHz) were adopted. For the mechanical stability test, the electrochemical impedance changes according to three folding methods (kinked, folded, and sulcus), including the original state of the device, were recorded. Impedance distribution and error bars were plotted based on 30 recording channels.

Neuron Hoechst and PI Staining Test: For primary cell culture, 8 weeks of adult mice were perfused with 0.9% normal saline and sacrificed whole brain without olfactory bulb and cerebellum in Dulbecco's PBS. The cerebral cortex was dissected in cold Hank's balanced salt solution. Cultured cells were placed in a neurobasal medium with a B-27 supplement. For cell viability analysis, 2×10^6 mL⁻¹ cells were placed in a four-well poly-D-lysine-coated slide. Hoechst 33 342 (1 μg mL⁻¹; Thermo) and PI (10 μg mL⁻¹; Sigma) were treated for 15 min at room temperature and washed out with PBS thrice. A 24 × 50 mm microscope cover glass was placed on a culture slide using a mounting solution. Stained cells were imaged by LSM700 (Zeiss).

Long-Term Biocompatibility Test in Living Body of the Rat: To test the biocompatibility of MRI-com PEDOT in a living body for a long period of time, three rats were anesthetized with sodium pentobarbital [50 mg kg⁻¹, intraperitoneal (i.p.) injection] and placed in a stereotaxic frame. After the incision in the lambda region of the parietal region without opening the skull, the MRI-com PEDOT was implanted into the brain with sliding the film between the bone and the dura mater. The MRI-com PEDOT was placed on the motor cortex and the gap in the bone created for insertion was sealed with bone wax and the skin sutured. During 1, 2, and 4 weeks after the insertion of PEDOT:PSS, rats were regularly monitored for signs of discomfort, illness, or adverse events, and data related to body weight, clinical signs, and other relevant observations were observed to be free of abnormalities. Rats were sacrificed and perfused with normal saline (0.9% NaCl). The biocompatibility of PEDOT:PSS was evaluated, focusing on the following aspects:

- 1) Fluid drainage: An adverse event may cause an inflammatory exudate to build up in the tissue. This can lead to fluid leakage from the insertion site or the formation of an abscess.
- 2) Lipid aggregation
- 3) Granuloma formation: If an adverse event occurs, a granuloma, a mass of immune cells that forms in response to a foreign body, may be observed at the site.
- 4) Systemic symptoms: The development of a systemic inflammatory response depends on the severity of the adverse event. If the adverse event is more extensive, the systemic inflammatory response may increase, resulting in systemic symptoms.

Electromagnetic Heating Simulation: The electromagnetic heating was simulated in COMSOL Multiphysics by coupling the electromagnetic waves (frequency domain) module with the Bioheat Transfer module for the brain tissue phantom (or the Heat Transfer in Solids module for the Pt and PEDOT:PSS electrodes). The electromagnetic waves were produced by the lumped port kept nearby the brain phantom, enclosed by a perfectly matched layer. The electric field E could be solved from the following electromagnetic waves propagation equation

$$\nabla \times \frac{1}{\mu_r} (\nabla \times E) - k_0^2 \left(\epsilon_r - \frac{j\sigma}{\omega\epsilon_0} \right) E = 0 \quad (6)$$

where μ_r and ϵ_r are the relative permeability and permittivity of the medium, respectively, k_0 is the wavenumber, ω is the frequency of the wave propagation, and σ is the electrical conductivity of the medium. The SAR is directly related to the generated electric field E in the brain phantom

$$\text{SAR} = \frac{\sigma |E|^2}{2\rho} \quad (7)$$

where ρ is the density of the medium or the brain phantom here. The Pt electrode shows higher SAR across the brain tissue than PEDOT:PSS and a peak of 53.4 from the Pt electrode is 117% higher than that of 24.6 from the PEDOT:PSS (Figure 2). The generated heat Q in the brain phantom raises the temperature T according to the following heat transport equation

$$\rho C_p u \cdot \nabla T + \nabla \cdot (-k \nabla T) = Q + \rho_b C_{p,b} \omega_b (T_b - T) + Q_{\text{met}} \quad (8)$$

where C_p is the specific heat capacity at constant stress, u is the velocity vector, k is the thermal conductivity, ρ_b is the density of blood, $C_{p,b}$ is the specific heat of blood, ω_b is the blood perfusion rate, T_b is the arterial blood temperature, and Q_{met} is the metabolic heat source. As the contributions from Q_{met} , T_b , and u remain the same for both electrodes, they are neglected in the current simulation without loss of generality. Due to a higher generated heat, Pt electrodes give higher temperature and heat flux in brain phantom than PEDOT:PSS electrodes after solving the heat transport equation. In particular, the peak temperature of 1.9 K from the Pt electrodes is 72% higher than that of 1.1 K from the PEDOT:PSS electrodes.

Electromagnetic Wave Compatibility Simulation Test: Ansys HFSS simulation tool (version 2021, R2) was used to confirm that the MRI-com PEDOT electrode was not affected by the electromagnetic field signal of the MRI scanner. All tests were conducted by selecting 300 MHz as a representative among the frequencies used with a thickness of 100 μm was placed in the center of a square waveguide with a frequency of ≥ 300 MHz as the cutoff frequency of the TE₁₀ mode. For more accurate results, the material and electrical properties of MRI-com PEDOT were set as simulation parameter values (relative permittivity: 1000, relative permeability: 0.9953, bulk conductivity: 196.1 S m⁻¹, dielectric loss tangent: 0.05, mass density: 1131.2 kg m⁻³). In the case of the Pt electrode, the reference parameters in the tool were used.

In Vitro RF-Induced Heat Measurement: Device heating temperature measurement by RF was measured with MRI-com temperature sensors inside a 9.4T Biospec small bore scanner (Bruker Biospin, Germany). First, a Pt electrode array and an MRI-com PEDOT were placed on 0.9% agarose gel, and contact was made with the temperature sensor inside the MRI. During the next 30 min of scanning time, imaging was stopped once every 5 min, and the changing temperature was observed.

In Vivo MRI Acquisition: In vivo MRI acquisition was conducted with a 9.4T Biospec small bore scanner. For the in vivo MRI compatibility test, the somatosensory cortex of male Sprague–Dawley rats (250–300 g) was imaged by the FLASH MRI method. After shimming and tuning, gradient echo sequence images were obtained for positioning. The imaging parameters of FLASH MRI were scanning slice: 15, TR: 200 ms, TE: 6 ms, FA: 30.0°, TA: 1 min 42 s 400 ms, SI: 0.2/0.2 mm, field of view: 3.5 cm, and matrix: 256 × 256. For MEMRI acquisition, the neuropathic pain model (control) and the MCS model were obtained with the same imaging. Anatomical images were obtained with the rapid acquisition with the relaxation enhancement method. During image acquisition, real-time changes in body temperature and respiratory rate of the rat model were measured by sensors in the scanner. During MEMRI acquisition, Mn-enhanced regions of the brain were acquired and images were analyzed using Paravision software (version 5.0, Bruker Biospin).

Animal Preparation: Male Sprague–Dawley rats weighing 250 to 300 g (Harlan, Koatec, Pyeongtaek, Korea) were used in all experiments. Three rats were housed per cage and allowed free water and food access. All rats were housed under 12 h light/dark cycle-controlled conditions in the Association for Assessment and Accreditation of Laboratory Animal Care-approved animal facilities. All protocols followed the ARRIVE guidelines, and the experiments were approved by the Institutional Animal Care and Use Committee of Yonsei University Health System (permit no. 2020-0316).

Neuropathic Surgery: Nerve injury was induced as described previously (Lee, Won, Baik, Lee, and Moon, 2000) after the acclimation period. Rats were anesthetized with a mixture of O₂ (2 L min⁻¹) and isoflurane using a 5% vaporizer. For stable anesthesia, isoflurane concentration was reduced by 2%. The incision in the skin and muscles was performed, and the left sciatic nerve was exposed. Tibial and sural nerves derived from the sciatic nerve were tightly ligated using a 5-0 black silk and transected, whereas the common peroneal nerve was uninjured. Sham surgery was identically performed without nerve transection.

Device Implantation and MCS: On postoperative day 14, rats were anaesthetized with sodium pentobarbital (50 mg kg⁻¹, intraperitoneal [i.p.] injection) and placed into the stereotaxic frame. MRI-com PEDOT was directly put on the brain cortex of the brain after the skull and dura mater were carefully removed into rectangles (from the contralateral side

of the operated hind paw, from anterior 2 mm to posterior 3 mm based on bregma, with a width of 5 mm). Recording channels were placed on S1HL following a previous study (Cha, Chae, Bai, and Lee, 2017) and fully covered the target region. Saline-soaked cotton balls were placed on the cortex to prevent drying. For electrode fixation, dental cement covered the electrode.

Electrophysiological Recording and MCS: To measure evoked electrophysiological potentials by HPS, a 30-channel MRI-com PEDOT was placed over the somatosensory region of the right cerebral cortex of a neuropathic rat model. At the same time, the cortex stimulating electrode was placed above the primary motor cortex (M1). All electrophysiological signal recording and electrical stimulation from the brain were performed using the Intan recording system (Intan RHS M4200; Intan Technologies, Los Angeles, CA, USA). Digitized signals (sampling rate: 30 kS s⁻¹, amplified bandwidth: 0.1–6000 Hz, notch filter: 60 Hz) obtained from the Intan recording system were extracted and graphed by the customized MATLAB code. For M1 stimulation, the previously studied stimulating parameter was used for all experiments (current intensity: 50 μA, biphasic symmetric and cathodic leading current, stimulating frequency: 50 Hz, phase duration: 300 μs). The neuropathic pain group underwent the same procedure without any electrical stimulation. For 2D color mapping of electrophysiological signals, the customized MATLAB code was used to change the raw voltage data to the corresponding colors (voltage range: –100 to 500 μV).

Agent Administration: Immediately after electrode placement, surgery for the preparation of agent administration was conducted as described previously (Cha, Choi, Kim, and Lee, 2020). The right ventral aspect of the neck was exposed by skin incision, and the common carotid artery (CCA), ECA, and internal carotid artery (ICA) were gently revealed. ICA and CCA were temporarily ligated, whereas a small incision was made in ECA to insert a polyethylene tubing 10 (PE-10). To open the BBB for agent absorption, 20% D-mannitol solution (35 ± 2 °C, 5 mL kg⁻¹; Dai Han Pharm, Seoul, Korea) was infused after PE-10 insertion. For MRI, 20 mM manganese chloride (MnCl₂·4H₂O; Sigma, St. Louis, MO, USA) was injected via ECA. All infusions were injected at 150 μL min⁻¹ using a syringe pump (22 Infusion Syringe Pump; Harvard Apparatus, Holliston, MA, USA). Electric stimulations (1.5 mA, 2 Hz, 1 ms width; A385; WPI, Sarasota, FL, USA) were subjected to the left hind paw for noxious stimulation during MnCl₂.

Animal Surgery for Simultaneous Electrophysiology and Optogenetics: For animal experiments, the Korea Institute of Science and Technology approved all animal procedures conducted in accordance with the ethical standards specified in the Animal Care and Use Guidelines (KIST-2021-046). MRI-com PEDOT was tested in adult male transgenic mice (C57BL6 Thy1-ChR2-YFP; 8–10 weeks, 25–30 g) and adult male WT mice (C57BL6; 8–10 weeks, 25–30 g). For electrophysiological measurements and optogenetics, transgenic mice were anesthetized with urethane (1.5 g kg⁻¹, i.p. injection) and placed in a stereotaxic device (David Kopf Instruments, USA). For device implantation, the dura mater of the somatosensory cortex of the right cerebral cortex was slightly eliminated.

Electrophysiological Recording with Optogenetic Stimulation: Neural signals evoked by optogenetic stimulation were obtained using an Intan recording system (Intan RHD 2132; Intan Technologies). First, an optical fiber with a diameter of 105 μm was placed directly above the target electrode of one of the Pt electrodes arrays and MRI-com PEDOT attached to the somatosensory cortex of a transgenic/WT mouse. A 473 nm blue laser with a light pulse density of 115.55 mW mm⁻² was directly illuminated onto the surface of the target electrode by an optical fiber, and electrophysiological signals activated by the laser were simultaneously recorded. The square wave frequency of the blue laser was 12.5% duty cycle, pulse duration of 50 ms, and stimulating frequency of 5 Hz. Digitized signals (sampling rate: 20 kS s⁻¹, amplified bandwidth: 0.1–6000 Hz, notch filter: 60 Hz) obtained from the Intan recording system were extracted and graphed by the customized MATLAB code.

Statistical Analysis: All electrochemical properties (impedance and phase plot) were presented as the mean ± standard deviation (*n* = 30 electrodes). To confirm the significance of the reduction effect of MCS on neuropathic pain, the statistical tool SPSS was used. For statistical

analysis, an unpaired *t*-test was used to analyze the differences between the two groups.

Supporting Information

Supporting Information is available from the Wiley Online Library or from the author.

Acknowledgements

Y.U.C. and K.K. contributed equally to this work. This work acknowledges the support from The National Research Foundation of Korea grant no. NRF 2019R1A2C2086085 and NRF-2021R1A4A1031437 (Y.W.C., K.J.Y.) and The Korean Government MSIT grant NRF 2020R1A2C3008481 (K.K., M.C.). The author byline and Acknowledgements were updated after initial online publication. [Correction added on January 3, 2024, after first online publication: the figure for the graphical abstract has been exchanged.]

Conflict of Interest

The authors declare no conflict of interest.

Data Availability Statement

The data that support the findings of this study are available from the corresponding author upon reasonable request.

Keywords

MRI compatible neural implants, neuropathic pain alleviation, poly(3,4-ethylenedioxythiophene):poly(styrene sulfonate) transparent electrodes

Received: September 10, 2023
Published online: October 27, 2023

- [1] I. Mastoris, H. G. C. V. Spall, S. H. Sheldon, R. C. Pimentel, L. Steinkamp, Z. Shah, S. M. Al-Khatib, J. P. Singh, A. J. Sauer, *J. Card. Failure* **2022**, *28*, 991.
- [2] E. McGlynn, V. Nabaei, E. Ren, G. Galeote-Checa, R. Das, G. Curia, H. Heidari, *Adv. Sci.* **2021**, *8*, 2002693.
- [3] Y. Cho, S. Park, J. Lee, K. J. Yu, *Adv. Mater.* **2021**, *33*, 2005786.
- [4] J. A. Frank, M.-J. Antonini, P. Anikeeva, *Nat. Biotechnol.* **2019**, *37*, 1013.
- [5] J. Shi, Y. Fang, *Adv. Mater.* **2019**, *31*, 1804895.
- [6] G. Hong, C. M. Lieber, *Nat. Rev. Neurosci.* **2019**, *20*, 330.
- [7] S. M. Won, E. Song, J. T. Reeder, J. A. Rogers, *Cell* **2020**, *181*, 115.
- [8] S. Jiang, D. C. Patel, J. Kim, S. Yang, W. A. Mills III, Y. Zhang, K. Wang, Z. Feng, S. Vijayan, W. Cai, *Nat. Commun.* **2020**, *11*, 6115.
- [9] Y. Liu, V. R. Feig, Z. Bao, *Adv. Healthcare Mater.* **2021**, *10*, 2001916.
- [10] K. Sugie, K. Sasagawa, M. C. Guinto, M. Haruta, T. Tokuda, J. Ohta, *Electron. Lett.* **2019**, *55*, 729.
- [11] L. Tian, B. Zimmerman, A. Akhtar, K. J. Yu, M. Moore, J. Wu, R. J. Larsen, J. W. Lee, J. Li, Y. Liu, B. Metzger, S. Qu, X. Guo, K. E. Mathewson, J. A. Fan, J. Cornman, M. Fatina, Z. Xie, Y. Ma, J. Zhang, Y. Zhang, F. Dolcos, M. Fabiani, G. Gratton, T. Bretl, L. J. Hargrove, P. V. Braun, Y. Huang, J. A. Rogers, *Nat. Biomed. Eng.* **2019**, *3*, 194.

- [12] L. Lu, X. Fu, Y. Liew, Y. Zhang, S. Zhao, Z. Xu, J. Zhao, D. Li, Q. Li, G. B. Stanley, X. Duan, *Nano Lett.* **2019**, *19*, 1577.
- [13] N. B. Babaroud, M. Palmar, A. I. Velea, C. Coletti, S. Weingärtner, F. Vos, W. A. Serdijn, S. Vollebregt, V. Giagka, *Microsyst. Nanoeng.* **2022**, *8*, 107.
- [14] F. Fallegger, G. Schiavone, E. Pirondini, F. B. Wagner, N. Vachicouras, L. Serex, G. Zegarek, A. May, P. Constanthin, M. Palma, M. Khoshnevis, D. Van Roost, B. Yvert, G. Courtine, K. Schaller, J. Bloch, S. P. Lacour, *Adv. Sci.* **2021**, *8*, 2003761.
- [15] F. Rocchi, C. Canella, S. Noei, D. Gutierrez-Barragan, L. Coletta, A. Galbusera, A. Stuefer, S. Vassanelli, M. Pasqualetti, G. Iurilli, S. Panzeri, A. Gozzi, *Nat. Commun.* **2022**, *13*, 1056.
- [16] T.-L. Wu, P.-F. Yang, F. Wang, Z. Shi, A. Mishra, R. Wu, L. M. Chen, J. C. Gore, *Nat. Commun.* **2019**, *10*, 1416.
- [17] D. Arimura, K. Shinohara, Y. Takahashi, Y. K. Sugimura, M. Sugimoto, T. Tsurugizawa, K. Marumo, F. Kato, *Front. Neural Circuits* **2019**, *13*, 58.
- [18] J. B. Erhardt, E. Fuhrer, O. G. Gruschke, J. Leupold, M. C. Wapler, J. Hennig, T. Stieglitz, J. G. Korvink, *J. Neural Eng.* **2018**, *15*, 041002.
- [19] L. Zrinzo, F. Yoshida, M. I. Hariz, J. Thornton, T. Foltynie, T. A. Yousry, P. Limousin, *World Neurosurg.* **2011**, *76*, 164.
- [20] L. Winter, F. Seifert, L. Zilberti, M. Murbach, B. Ittermann, *J. Magn. Reson. Imaging* **2021**, *53*, 1646.
- [21] R. Srinivasan, C. W. So, N. Amin, D. Jaikaransingh, F. D'arco, R. Nash, *Clin. Radiol.* **2019**, *74*, 972e9.
- [22] D. Sayed, K. Chakravarthy, K. Amirdelfan, H. Kalia, K. Meacham, P. Shirvalkar, S. Falowski, E. Petersen, J. M. Hagedorn, J. Pope, *Neuro-modulation: Technol. Neural Interface* **2020**, *23*, 893.
- [23] J. F. Schenck, *Med. Phys.* **1996**, *23*, 815.
- [24] Y. Zhang, S. Le, H. Li, B. Ji, M.-H. Wang, J. Tao, J.-Q. Liang, X.-Y. Zhang, X.-Y. Kang, *Biosens. Bioelectron.* **2021**, *194*, 113592.
- [25] K. El Bannan, W. Handler, B. Chronik, S. P. Salisbury, *J. Magn. Reson. Imaging* **2013**, *38*, 411.
- [26] R. Feiner, T. Dvir, *Nat. Rev. Mater.* **2017**, *3*, 17076.
- [27] S. P. Lacour, G. Courtine, J. Guck, *Nat. Rev. Mater.* **2016**, *1*, 16063.
- [28] R. A. Green, N. H. Lovell, G. G. Wallace, L. A. Poole-Warren, *Biomaterials* **2008**, *29*, 3393.
- [29] J. Y. Lee, S. H. Park, Y. Kim, Y. U. Cho, J. Park, J.-H. Hong, K. Kim, J. Shin, J. E. Ju, I. S. Min, *npj Flexible Electron.* **2022**, *6*, 86.
- [30] G. Kaur, R. Adhikari, P. Cass, M. Bown, P. Gunatillake, *RSC Adv.* **2015**, *5*, 37553.
- [31] M. Jia, M. Rolandi, *Adv. Healthcare Mater.* **2020**, *9*, 1901372.
- [32] M. Han, E. Yildiz, H. N. Kaleli, S. Karaz, G. O. Eren, I. B. Dogru-Yuksel, E. Senses, A. Sahin, S. Nizamoglu, *Adv. Healthcare Mater.* **2022**, *11*, 2102160.
- [33] L. V. Kayser, D. J. Lipomi, *Adv. Mater.* **2019**, *31*, 1806133.
- [34] Y. Liang, A. Offenhäusser, S. Ingebrandt, D. Mayer, *Adv. Healthcare Mater.* **2021**, *10*, 2100061.
- [35] G. Dijk, H. J. Ruigrok, R. P. O'Connor, *Adv. Mater. Interfaces* **2020**, *7*, 2000675.
- [36] G. Dijk, H. J. Ruigrok, R. P. O'Connor, *Adv. Mater. Interfaces* **2021**, *8*, 2100214.
- [37] M. Ganji, A. Tanaka, V. Gilja, E. Halgren, S. A. Dayeh, *Adv. Funct. Mater.* **2017**, *27*, 1703019.
- [38] Y. U. Cho, J. Y. Lee, U.-J. Jeong, S. H. Park, S. L. Lim, K. Y. Kim, J. W. Jang, J. H. Park, H. W. Kim, H. Shin, H. Jeon, Y. M. Jung, I.-J. Cho, K. J. Yu, *Adv. Funct. Mater.* **2022**, *32*, 2105568.
- [39] M. Vosgueritchian, D. J. Lipomi, Z. Bao, *Adv. Funct. Mater.* **2012**, *22*, 421.
- [40] Z. Ahmad, A. W. Azman, Y. F. Buys, N. Sarifuddin, *Mater. Adv.* **2021**, *2*, 7118.
- [41] H. Shi, C. Liu, Q. Jiang, J. Xu, *Adv. Electron. Mater.* **2015**, *1*, 1500017.
- [42] Y.-J. Lin, W.-S. Ni, J.-Y. Lee, *J. Appl. Phys.* **2015**, *117*, 215501.
- [43] T.-C. Wei, S.-H. Chen, C.-Y. Chen, *Mater. Chem. Front.* **2020**, *4*, 3302.
- [44] M. Cha, S. W. Um, M. Kwon, T. S. Nam, B. H. Lee, *Sci. Rep.* **2017**, *7*, 7986.
- [45] M. Cha, K. H. Lee, B. H. Lee, *Sci. Rep.* **2020**, *10*, 943.
- [46] M. Cha, Y. Ji, R. Masri, *J. Pain* **2013**, *14*, 260.
- [47] D.-W. Park, J. P. Ness, S. K. Brodnick, C. Esquibel, J. Novello, F. Atry, D.-H. Baek, H. Kim, J. Bong, K. I. Swanson, *ACS Nano* **2018**, *12*, 148.
- [48] M. Lee, S. Lee, J. Kim, J. Lim, J. Lee, S. Masri, S. Bao, S. Yang, J.-H. Ahn, S. Yang, *NPG Asia Mater.* **2021**, *13*, 65.
- [49] J. Zhang, X. Liu, W. Xu, W. Luo, M. Li, F. Chu, L. Xu, A. Cao, J. Guan, S. Tang, X. Duan, *Nano Lett.* **2018**, *18*, 2903.
- [50] O. Beuf, A. Briguët, M. Lissac, R. Davis, *J. Magn. Reson., Ser. B* **1996**, *112*, 111.
- [51] K. B. Baker, J. A. Tkach, J. A. Nyenhuis, M. Phillips, F. G. Shellock, J. Gonzalez-Martinez, A. R. Rezai, *J. Magn. Reson. Imaging* **2004**, *20*, 315.
- [52] L. M. Angelone, A. Potthast, F. Segonne, S. Iwaki, J. W. Belliveau, G. Bonmassar, *Bioelectromagnetics* **2004**, *25*, 285.
- [53] T. G. Reese, O. Heid, R. M. Weisskoff, V. J. Wedeen, *Magn. Reson. Med.* **2003**, *49*, 177.
- [54] C. T. M. Choi, A. Konrad, *IEEE Trans. Magn.* **1991**, *27*, 4227.
- [55] L. Golestanirad, E. Kazemivalipour, B. Keil, S. Downs, J. Kirsch, B. Elahi, J. Pilitsis, L. L. Wald, *PLoS One* **2019**, *14*, e0220043.
- [56] T. Lottner, S. Reiss, S. B. Rieger, M. Schuettler, J. Fischer, L. Bielak, A. C. Özen, M. Bock, *Neuroimage* **2022**, *264*, 119691.
- [57] B. A. Al-Asbahi, S. M. H. Qaid, A. G. El-Shamy, *J. Ind. Eng. Chem.* **2021**, *100*, 233.
- [58] A. Pasha, A. S. Roy, M. Murugendrapa, O. A. Al-Hartomy, S. Khasim, *J. Mater. Sci.: Mater. Electron.* **2016**, *27*, 8332.
- [59] A. Pasha, S. Khasim, O. A. Al-Hartomy, M. Lakshmi, K. G. Manjunatha, *RSC Adv.* **2018**, *8*, 18074.
- [60] L. Garcia-Larrea, R. Peyron, *Neuroimage* **2007**, *37*, S71.
- [61] C. Hamani, E. T. Fonoff, D. C. Parravano, V. A. Silva, R. Galhardoni, B. A. Monaco, J. Navarro, L. T. Yeng, M. J. Teixeira, D. C. De Andrade, *Brain* **2021**, *144*, 2994.
- [62] X. Moisset, J.-P. Lefaucheur, *Rev. Neurol.* **2019**, *175*, 51.
- [63] Z. Chen, N. Boyajian, Z. Lin, R. T. Yin, S. N. Obaid, J. Tian, J. A. Brennan, S. W. Chen, A. N. Miniovich, L. Lin, Y. Qi, X. Liu, I. R. Efimov, L. Lu, *Adv. Mater. Technol.* **2021**, *6*, 2100225.
- [64] L. Zou, H. Tian, S. Guan, J. Ding, L. Gao, J. Wang, Y. Fang, *Nat. Commun.* **2021**, *12*, 5871.
- [65] Y. U. Cho, S. L. Lim, J.-H. Hong, K. J. Yu, *npj Flexible Electron.* **2022**, *6*, 53.
- [66] T. D. Y. Kozai, A. L. Vazquez, *J. Mater. Chem. B* **2015**, *3*, 4965.